PASJ: Publ. Astron. Soc. Japan **60**, S453–S466, 2008 December 25

Supernova Remnants in the AKARI IRC Survey of the Large Magellanic Cloud

Ji Yeon SEOK,[1] Bon-Chul KOO,[1] Takashi ONAKA,[2] Yoshifusa ITA,[3] Ho-Gyu LEE,[1] Jae-Joon LEE,[4] Dae-Sik MOON,[5] Itsuki SAKON,[2] Hidehiro KANEDA,[6] Hyung Mok LEE,[1] Myung Gyoon LEE,[1] Sung Eun KIM[7]

[1]*Department of Physics and Astronomy, Seoul National University, Seoul 151-742, Korea*
jyseok@astro.snu.ac.kr; koo@astrohi.snu.ac.kr; hglee@astro.snu.ac.kr; hmlee@astro.snu.ac.kr; mglee@astro.snu.ac.kr

[2]*Department of Astronomy, Graduate School of Science, The University of Tokyo, Bunkyo-ku, Tokyo 113-0033*
onaka@astron.s.u-tokyo.ac.jp; isakon@maitta.astron.s.u-tokyo.ac.jp

[3]*National Astronomical Observatory of Japan, 2-21-1 Osawa, Mitaka, Tokyo 181-8588*
yoshifusa.ita@nao.ac.jp

[4]*Department of Astronomy and Astrophysics, Pennsylvania State University, 525 Davey Laboratory, University Park, PA 16802, USA*
lee@astro.psu.edu

[5]*Department of Astronomy and Astrophysics, University of Toronto, Toronto, ON M5S 3H4, Canada*
moon@astro.utoronto.ca

[6]*Institute of Space and Astronautical Science, Japan Aerospace Exploration Agency, Sagamihara, Kanagawa 229-8510*
kaneda@ir.isas.jaxa.jp

[7]*Department of Astronomy and Space Science, Sejong University, Seoul 143-747, Korea*
sek@sejong.ac.kr

(Received 2008 June 1; accepted 2008 October 14)

Abstract

We present a near- to mid-infared study of supernova remnants (SNRs) using the AKARI IRC Survey of the Large Magellanic Cloud (LMC). The LMC survey observed about a 10 square degree area of the LMC in five bands centered at 3, 7, 11, 15, and 24 μm using the Infrared Camera (IRC) aboard AKARI. The number of SNRs in the survey area is 21, which is about a half of the known LMC SNRs. We systematically examined AKARI images and identified eight SNRs with distinguishable infrared emission. All of them were detected at $\gtrsim 10\,\mu$m and some at 3 and 7 μm, too. We present their AKARI images and fluxes. In the $11/15\,\mu$m versus $15/24\,\mu$m color–color diagram, the SNRs appear to be aligned along a modified blackbody curve, representing thermal emission from dust at temperatures of between 90 and 190 K. There is a good correlation between the 24 μm and X-ray fluxes of the SNRs. It was also found that there is a good correlation between the 24 μm and radio fluxes even if there is no direct physical connection between them. We considered the origin of the detected mid-infrared emission in individual SNRs. We conclude that the mid-infrared emissions in five SNRs that show morphologies similar to the X-rays are dominated by thermal emission from hot dust heated by X-ray emitting plasma. Their $15/24\,\mu$m color temperatures are generally higher than the Spitzer $24/70\,\mu$m color temperatures, which suggests that a single-temperature dust model cannot describe the full spectral energy distribution (SED) of the SNRs. It also implies that our understanding of the full SED is essential for estimating the dust destruction rate of grains by SNR shocks.

Key words: ISM: dust, extinction — ISM: individual (0509−67.5, 0519−69.0, N 132 D, N 49 B, N 49, SN 1987A, N 157 B, 0548−70.4) — Magellanic Clouds — supernova remnants

1. Introduction

A supernova (SN) explosion is one of the most energetic events in the Universe, ejecting various elements of stellar mass with enormous energy. It plays an important role in the evolution of the interstellar medium (ISM) by generating strong shocks, which heat and accelerate the medium and destroy dust grains. A significant amount of dust grains may also be formed in the SN ejecta. These processes can be studied by observing the remnants of the explosion, supernova remnants (SNRs), at various wavelengths. In particular, infrared (IR) observation can significantly improve our understanding on physical processes associated with dust grains, because they, either newly synthesized or swept-up by SN shocks, radiate essentially only in the IR. It is also useful to explore the nature of SNRs and their environments through atomic, ionic, and molecular lines in the IR, and also sometimes through synchrotron emission from relativistic electrons.

The Large Magellanic Cloud (LMC) contains more than forty radio / X-ray SNRs, and offers a unique opportunity for studying SNRs, owing to its location. At a distance of 51.4 kpc (Panagia 1999) far off from the galactic plane, we can see the detailed structure of SNRs without much confusion by foreground or background material. In spite of such advantages and the importance as our neighbor galaxy, IR studies on SNRs in the LMC have not flourished compared to radio or X-rays due to observational obstacles. The Infrared Astronomy Satellite (IRAS) opened an era of IR studies in the 1980s by detecting IR emission from a number of SNRs (Graham et al. 1987). The instrumental ability, such as spatial resolution and wavelength coverage, however, was not sufficient to reveal the nature of the IR emission from individual SNRs.

The Spitzer Space Telescope, launched in 2003, has made significant progress in this field. Using the recent Spitzer Survey of the LMC: Surveying the Agents of a Galaxy Evolution (SAGE: Meixner et al. 2006), it became possible to investigate almost the whole region of the LMC ($7 \times 7\,\mathrm{deg}^2$) at 3–8 μm and at 24–160 μm. In addition, a separate survey of 39 LMC SNRs was conducted to study the interstellar dust life-cycle in terms of ejecta formation by SNe and dust destruction by SNR blast waves (PI: K. Borkowski). Its preliminary results suggest that a substantial amount of small grains are destroyed in both Type Ia (Borkowski et al. 2006) and core-collapse SNRs (B. Williams et al. 2006). Williams, Chu, and Gruendl (2006) carried out Spitzer observations of six SNRs in the LMC, and found line emission to be a significant contributor to the IR emission. Tappe, Rho, and Reach (2006) reported on the detection of bright mid-infrared (MIR) emission together with the polycyclic aromatic hydrocarbon (PAH) features in the oxygen-rich SNR N 132 D using Spitzer imaging and spectroscopy.

Recently, the AKARI infrared space telescope, launched on 2006 February 21 (UT), has performed a large-scale survey of the LMC (Ita et al. 2008; see section 2). AKARI has continuous coverage of imaging from 2.5–26 μm, which is a powerful tool to investigate the IR trait of SNRs. In particular, the 11 and 15 μm bands are unique to AKARI, and could provide important information unobtainable with the Spitzer observations. In this paper, we report on the detection of IR emission in eight out of 21 SNRs in the AKARI IRC survey field. We present their images and show that there is a good correlation between the MIR and X-ray/radio fluxes. We discuss the origin of their MIR emission.

2. AKARI LMC Survey and SNR Identification

The data we used is from the AKARI large-scale survey of the Large Magellanic Cloud (PI: T. Onaka), one of the three AKARI large-scale survey programs. The survey was performed from 2006 May to 2007 July using the on-board instrument Infrared Camera (IRC: Onaka al. 2007). IRC has three channels: NIR/MIR-S channels sharing the same $10' \times 10'$ field-of-view and MIR-L channel observing the sky about $25'$ away from the NIR/MIR-S field-of-view. The survey covers about a $10\,\mathrm{deg}^2$ region of the LMC, which includes most of the major regions of the LMC in all three channels (figure 1). Areas near the boundary of this targeted area were covered in either NIR/MIR-S or MIR-L channel. The imaging observations were carried out in five bands: *N3* (2.7–3.8 μm), *S7* (5.9–8.4 μm), *S11* (8.5–13.1 μm), *L15* (12.6–19.4 μm), and *L24* (20.3–26.5 μm). The total integration time was 133 s for an *N3* band image and 147 s for the other band images (Ita et al. 2008), and the 5σ sensitivities per pointing were 16, 74, 132, 279, and 584 μJy in *N3*, *S7*, *S11*, *L15*, and *L24*, respectively (Onaka al. 2007). We processed the images by using the standard IRC imaging data reduction pipeline.[1] In addition to these imaging observations, near-infrared (NIR) low-resolution slit-less spectroscopy ($R \sim 20$) was performed for the same $10\,\mathrm{deg}^2$ region in 2–5 μm with the NIR prism spectroscopic mode (NP) of IRC. We also examined the spectroscopic data of individual SNRs. However, since most of them are not visible in this spectral range, and even the SNRs showing NIR spectra have difficulties to extract useful information due to confusion from background and/or nearby sources, we do not mention the NP results in this paper.

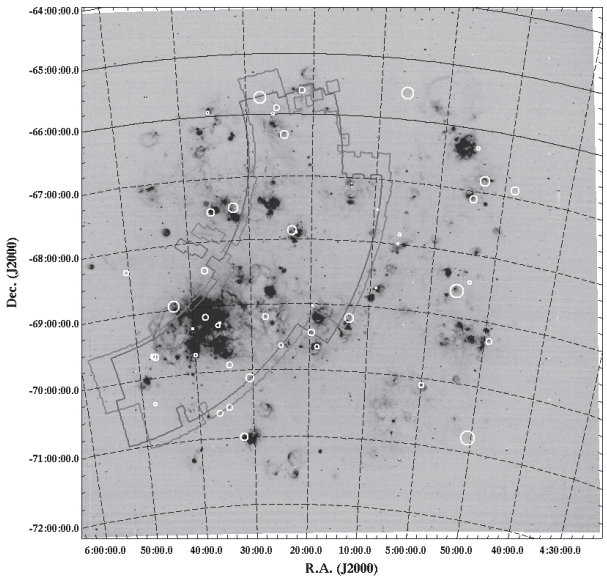

Fig. 1. Observed area of the AKARI IRC survey, overlaid on the Hα image of the Large Magellanic Cloud (Kim 1998). The dark gray and the light-gray lines indicate the survey area in the NIR/MIR-S and the MIR-L bands, respectively. Note that there is a discrepancy of the observed areas among the bands due to their separate field-of-views. The marked circles represent the location of the known SNRs and SNR candidates, and the size of each circle is proportional to that of the corresponding SNR.

Twenty one, previously-known LMC SNRs are included in the AKARI LMC survey area. Figure 1 shows their positions on the Hα image obtained by Kim (1998) together with the boundary of the area covered in the AKARI LMC survey. We examined whether there is IR emission associated with the SNRs. Some SNRs are embedded within IR-bright H II regions or H II complexes, such as 30 Doradus, so that a careful inspection was required to discriminate the SNR emission from the surrounding medium. The reference data that we used for confirming our SNR identification were the X-ray images from the Chandra Supernova Remnant Catalog (CSRC) page,[2] the radio images from 4.8 GHz survey using the Australia Telescope Compact Array (ATCA: Dickel et al. 2005), and optical images from the Magellanic Cloud Emission Line Survey (MCELS: Smith et al. 2000). Table 1 lists 21 SNRs in the survey area, and summarizes the results of the search. We have identified eight SNRs in total, which have associated IR emission in the NIR and/or MIR bands, including three Type Ia SNRs and five core-collapse SNRs (Type II SNRs for simplification, hereafter). Most of the identified SNRs have distinct shell-like features in the MIR-L bands as well as some

[1] AKARI IRC Data User's Manual ver. 1.3 ⟨http://www.ir.isas.jaxa.jp/AKARI/Observation/#IDUM⟩.

[2] ⟨http://hea-www.harvard.edu/ChandraSNR/⟩.

Table 1. SNRs in the AKARI LMC survey.*

SNR	RA (J2000.0)	Dec (J2000.0)	Size (′)	4.8 GHz flux (mJy)	Type	AKARI coverage	AKARI detection
(1)	(2)	(3)	(4)	(5)	(6)	(7)	(8)
0509−67.5	05:09:31	−67:31:17	0.56 × 0.56	22	Ia	A	*S11/L15/L24*
0513−69.2	05:13:14	−69:12:20	4.8 × 3.4	78	I?	B2	...
0519−69.0	05:19:35	−69:02:09	0.67 × 0.58	37	Ia	A	*S11/L15/L24*
0520−69.4	05:19:44	−69:26:08	3.1 × 2.7	28	?	C	...
SNR in N 44	05:23:07	−67:53:12	4.1 × 4.4	< 648	?	A	...
DEM L 175 A	05:24:20	−66:24:23	4.4 × 3.4	< 133	I?	A	...
N 132 D	05:25:04	−69:38:20	2.2 × 1.7	1625	II	B1	*S11/L15/L24*
N 49 B	05:25:25	−65:59:19	2.7 × 2.3	162	II	A	*S11/L15/L24*
N 49	05:26:00	−66:04:57	1.5 × 1.4	611	II	A	all bands
0528−69.2	05:27:39	−69:12:04	2.7 × 2.2	16	II?	A	...
DEM L 204	05:27:54	−65:49:38	5.2 × 4.9	38	II?	B1	...
0534−69.9	05:34:02	−69:55:03	2.6 × 2.2	26	Ia?	A	...
SN 1987 A	05:35:28	−69:16:11	0.04 × 0.04	33†	II	A	all bands
Honeycomb	05:35:46	−69:18:02	2.2 × 1.2	10	?	A	...
DEM L 249	05:36:07	−70:38:37	3.1 × 2.3	9	Ia?	C	...
N 157 B	05:37:49	−69:10:20	3.1 × 2.4	1042	II(Crab-like)	A	*N3/S11/L15/L24*
N 158 A	05:40:11	−69:19:55	1.3 × 1.1	341	II(Crab-like)	A	...
SNR in N 159	05:39:59	−69:44:02	2.0 × 1.8	1214	?	A	...
DEM L 316 B	05:46:59	−69:42:50	3.4 × 2.8	317‡	II	A	...
DEM L 316 A	05:47:22	−69:41:26	2.2 × 1.9	317‡	Ia?	A	...
0548−70.4	05:47:49	−70:24:54	2.0 × 1.8	6	Ia	A	*S11/L15/L24*

* Columns (1)–(4): SNR names, positions, and angular sizes from the MC SNR Atlas by R. Wiliiams (http://www.astro.uiuc.edu/projects/atlas/). Angular sizes are mostly in optical. The size of SN 1987A is a radius of the inner equatorial ring (Bouchet et al. 2006). Column (5): 4.8 GHz flux estimated from the radio image of Dickel et al. (2005) available at the NCSA Astronomy Digital Image Library. The statistical errors of SNRs are $\lesssim 5\%$, and limits are 3σ. Column (6): SNR type from mostly R. Williams et al. (1999) and other literatures. Except the two Crab-like SNRs, Type II SNRs are shell type SNRs of core-collapse SN origin. For unclear/undefined SNR types, question marks are used. Column (7): AKARI coverage states how completely the AKARI IRC LMC survey includes the SNR area in the IRC bands. A: all covered by AKARI in all bands, B1: wholly in the MIR-L and partially in the NIR/MIR-S, B2 : vice versa, and C: only partially in some bands. Column (8): AKARI bands in which the IR emission from the SNR is detected.

† Observed at 2003 February 14 (day 5846 after the SN explosion). A scaled flux to the day 7190 (56.5 mJy) is used for a further analysis (see subsection 4.2).

‡ Since DEM L 316 B and DEM L 316 A are located very closely, the total radio flux of the two SNRs is estimated.

related emission in the *S11* band. Only a few SNRs show any emission possibly associated with the SNR in shorter wave bands. Figures 2 and 3 show the AKARI MIR-band images of the identified eight SNRs, and figure 4 shows the AKARI *N3* and *S7* band images of the two SNRs (excluding SN 1987A) with the related NIR features.

3. Infrared Properties of SNRs

3.1. Morphologies and Fluxes

Most of the identified SNRs are visible in the *S11*, *L15*, and *L24* bands. In the *S11* band, however, the SNR features are confused by the foreground and background emissions, which might be dominated by strong PAH 11.3 μm band emission from dust. We subtracted this background emission using the *S7* band image, which is also dominated by the PAH emission from the background. We estimated the mean ratio of *S11* to *S7* surface brightness of the background emission in each SNR field from a pixel-to-pixel plot of *S11* versus *S7* brightness, and subtract the scaled *S7* image from the *S11* image, i.e., $S11-(a \times S7+b)$, where the scaling factors a and b range over 0.4–1.4 and 9–14 MJy/sr, respectively. The resulting "$S11-S7$" image shows the SNR features much more clearly than the original *S11* image. In figures 2 and 3, we show the *S11*, $S11-S7$, *L15*, and *L24* images of eight identified SNRs together with their Chandra X-ray images.

In all of the sources, we can see distinct MIR emission features at the position of SNRs in the *S11*, *L15*, and *L24* bands. The first five sources (0509−67.5, 0519−69.0, N 132 D, N 49 B, and N 49) show shell-like structures that are similar to the X-ray SNRs, so that the association of the IR emission with the SNRs is conclusive. The MIR brightness distribution appears to be correlated with the X-ray brightness distribution in general, but in 0519−69.0 and N 49, the morphologies are somewhat different, e.g., their peak positions do not coincide. SN 1987A is not resolved in our observation, but the positional coincidence verifies the association. N 157 B is a Crab-like SNR, and there is *no* detectable MIR emission associated

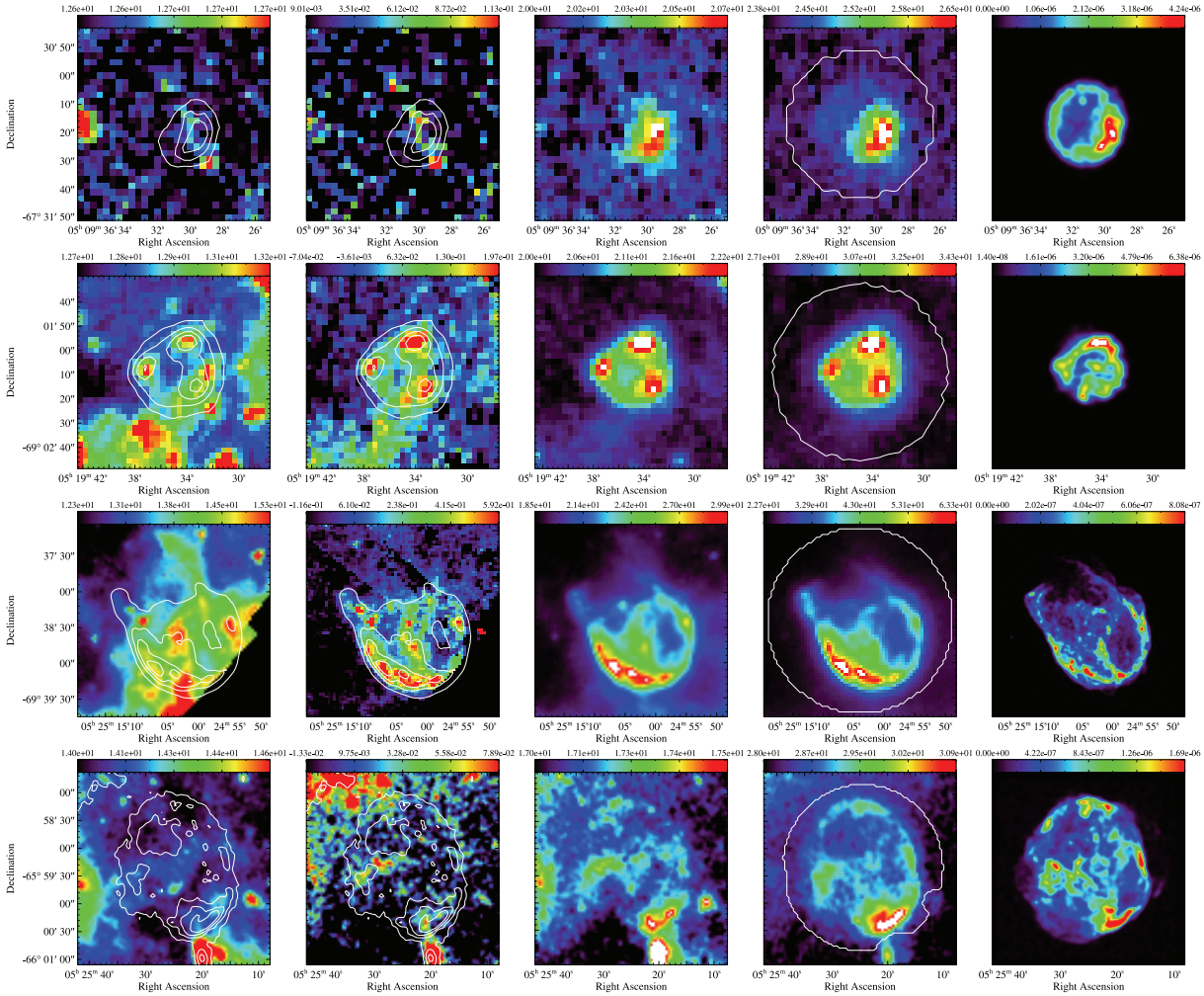

Fig. 2. From top to bottm: AKARI images of 0509−67.5, 0519−69.0, N 132 D, and N 49 B. For each SNR, *S11*, "*S11* − *S7*", *L15*, and *L24* images are shown together with their Chandra X-ray (0.3−2.1 keV) images for comparison. *S11* − *S7* images are made by subtracting the scaled *S7* images from the *S11* images (see text for details). The Chandra images are from the CSRC. The contours in the *S11* and *S11* − *S7* images show the brightness distribution of SNRs in the *L24* band, and the contours in the *L24* images represent the area used for flux derivations. For N 49 B, the images are smoothed with a two-pixel Gaussian profile. The unit on the color bar of the AKARI images are MJy/sr, and that of the Chandra are counts $\mathrm{cm}^{-2}\,\mathrm{s}^{-1}$.

with the X-ray/radio pulsar wind nebula (PWN).[3] (The very bright emission to the south of the remnant is associated with star-forming regions, not with the SNR.) But this remnant has bright, extended Hα emission with a strong peak to the east of the PWN (Chu et al. 1992), and a faint 'horseshoe-shaped' structure near to the center of the field corresponds to the bright optical filaments (see next); 0548−70.4 is located in a rather complicated field with several MIR sources around, but still the MIR emission corresponding to the X-ray bright interior can be clearly seen. The brightness distribution of the MIR emission, however, appears to be different from that of the X-rays. The limbs are barely visible only in the *L24* band. For all SNRs in figures 2 and 3, Spitzer obtained 24 μm images (Borkowski et al. 2006; B. Williams et al. 2006; R. Williams et al. 2006), and our *L24* images are consistent with them. The AKARI *S11* and *L15* images are new, and the fact that each SNR shows compatible morphologies in three bands suggests that the MIR emissions in these three bands are of the same origin.

In shorter wavebands, three SNRs are clearly visible: N 49, SN 1987A, and N 157 B. N 132 D, the MIR brightest SNR does not show any distinct NIR emission corresponding to the features seen in the MIR bands, which is partly due to its location in the complex area (cf. Tappe et al. 2006). The *N3* and *S7* images of N 49 and N 157 B are shown in figure 4 along with their Hα images. N 49 has a bright wedge-shaped feature in the eastern part of the remnant, which matches well with the bright optical filaments. N 157 B is contaminated by emission from the bright source below the remnant, but still we can identify the features corresponding to the optical filamentary structures, including the bright horseshoe-shaped one. The optical counterparts can be distinguished in all IRC bands except for *S7*. These *N3* and *S7* images are consistent with the Spitzer

[3] If we extrapolate the radio spectrum of the PWN (Lazendic et al. 2000), the expected surface brightness at the radio peak, $(\alpha, \delta) = (05^{\mathrm{h}}37^{\mathrm{m}}45^{\mathrm{s}}, -69^{\circ}10'11'')$, is estimated to be 2.7 and 3.0 MJy/sr at 7 and 11 μm, which is greater than the 2σ detection limit, 0.7 and 1.9 MJy/sr, in the *S7* and *S11* bands, respectively. This suggests that the PWN has a spectral break at a wavelength longer than 11 μm.

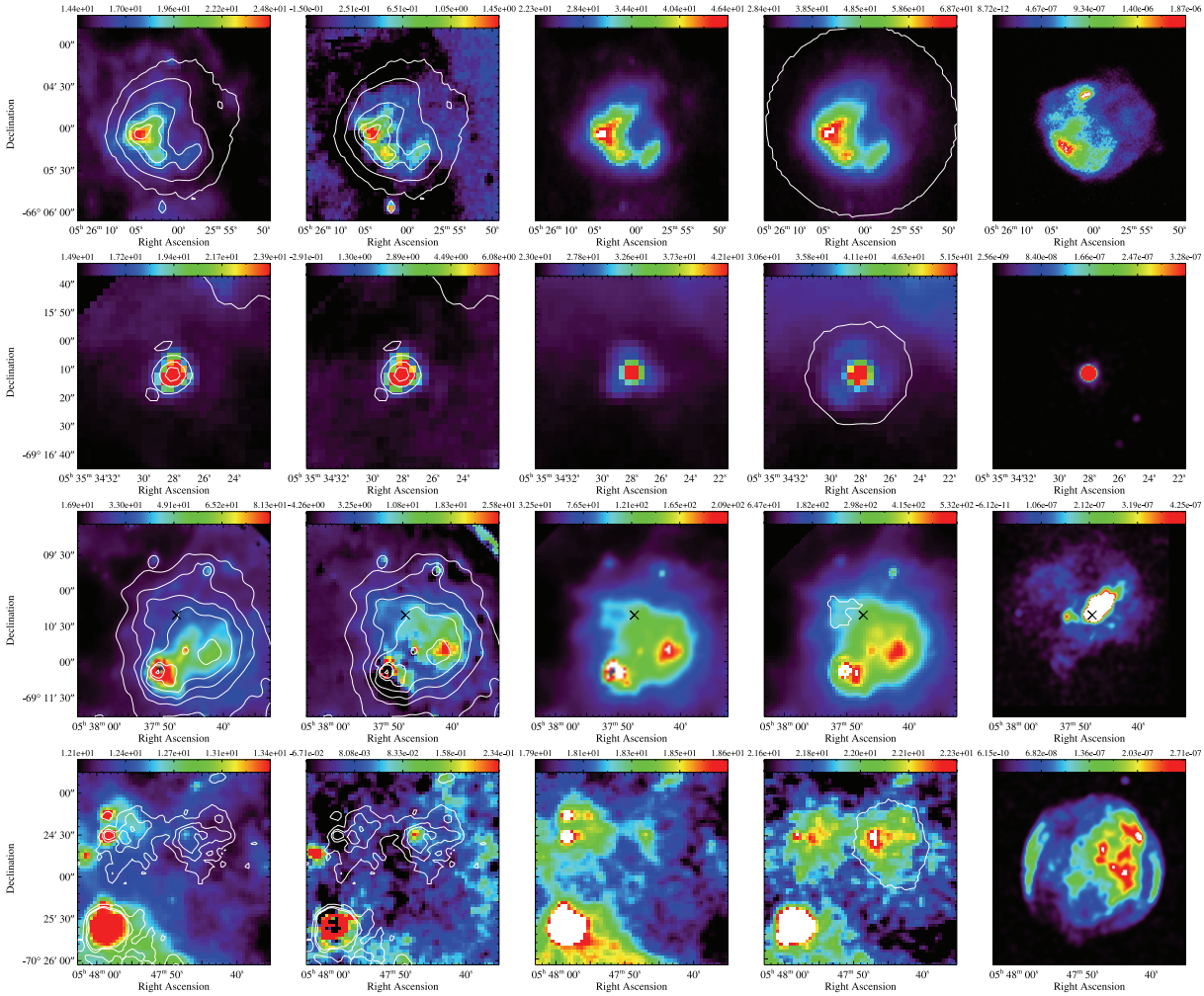

Fig. 3. From top to bottm: Same as figure 2, but for N 49, SN 1987A, N 157 B, and 0548−70.4. "×" marks on the third row represent the position of pulsar in N 157 B. The images of 0548−70.4 were smoothed with a two-pixel Gaussian. Note that for N 157 B and 0548−70.4, the flux has been extracted from the limited region due to the confusion (see subsection 3.1).

images, which have slightly higher resolution (R. Williams et al. 2006). We briefly describe the characteristics of each source in the Appendix.

For the identified SNRs, we derived their fluxes in each band (table 2). The *S11* fluxes were derived from the *S11*−*S7* images, except N 49 and SN 1987A, which show appreciable emission in the *S7* band. The areas used for flux estimation are marked in the *L24* images of figures 2 and 3. The fluxes were extracted from the entire SNR area, except for three SNRs: N 132 D, N 157 B, and 0548−70.4. N 132 D is incompletely covered in the NIR and MIR-S bands, so that we could obtain the total fluxes only in the MIR-L. Because the fraction of the uncovered area, however, is small, we estimated the total *S11* flux by first deriving the ratio of the *S11* to *L15* flux from the shared area and then by multiplying it to the total *L15* flux. N 157 B is confused by the southern star-forming regions, so we extract only the fluxes from the horseshoe-shape region in order to avoid any contamination from other sources. 0548−70.4 is located in a complicated area, and the background stars are located near the eastern rim.

Our measured IR fluxes are uncertain by 10−30% ($1\,\sigma$), considering the uncertainties in the measurements, background estimation, and the absolute calibration. For most sources, the error in the absolute calibration dominates, which is about 10% (see Koo et al. 2007). The IRC fluxes are those at reference wavelengths, assuming a flux distribution of $f_\lambda \propto \lambda^{-1}$.[1] We did not apply any color-correction since the origin of the IR emission can differ from source to source. All flux values that we employed for further analysis were not the color-corrected ones, except those described in subsection 5.1, where we consider the dust properties. The derived IRC fluxes are mostly consistent with the published Spitzer fluxes (e.g., Borkowski et al. 2006). For SN 1987A, Dwek et al. (2008) showed that its flux at 24 μm was $\sim$30 mJy on 2004 February 4 (day 6190) and increased by a factor of 2 after 947 days (day 7137). The AKARI spectrum was obtained from 2006 October 31 to November 4 (day 7190−7194), and the derived IRC fluxes are similar to those of the latest spectra with the Spitzer Infrared Spectrograph (IRS).

We compare the *L15* and *L24* fluxes of the identified SNRs in

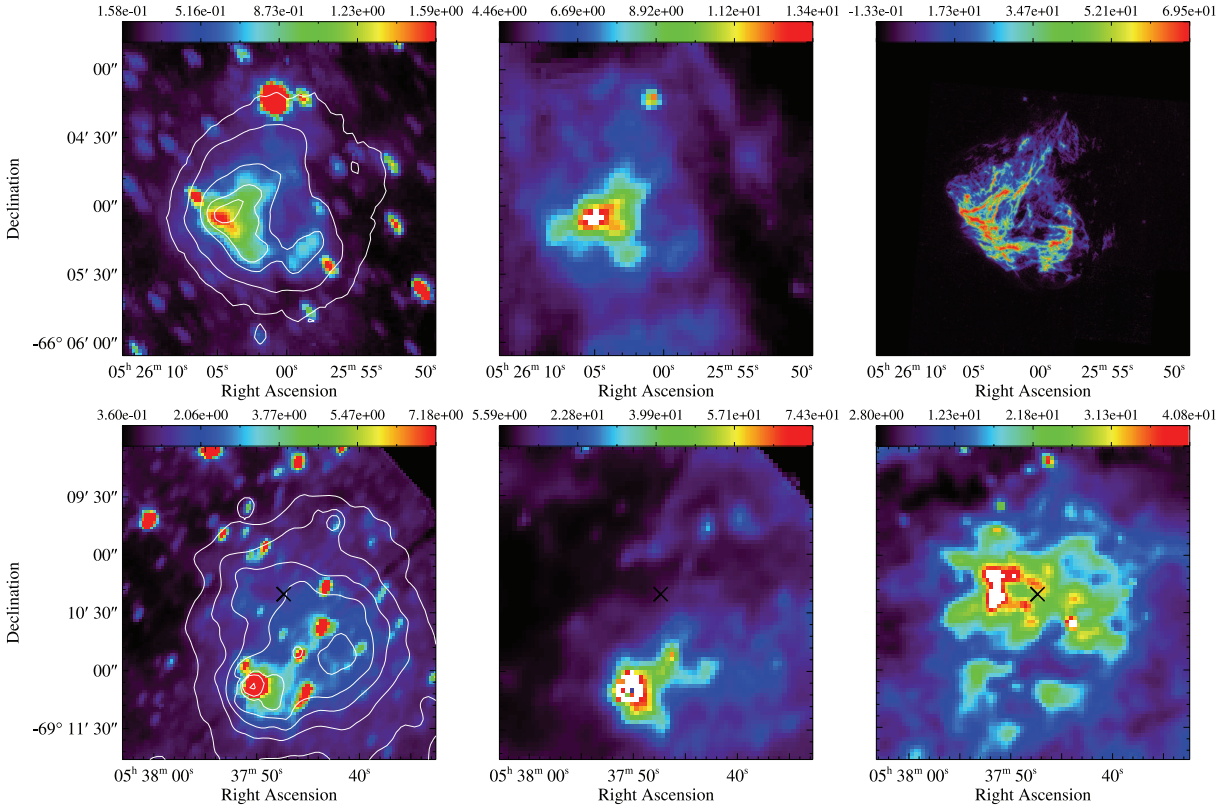

Fig. 4. *N3*, *S7*, and Hα images of N 49 (top) and N 157 B (bottom). These two (and SN 1987A are SNRs identified in these bands. The contours in the *N3* images show the brightness distribution of SNRs in the *L24* band. Optical images of N 49 and N 157 B are from the Hubble Space Telescope (HST) WFPC2 (Bilikova et al. 2007) and the CTIO Curtis Schmidt Telescope,[4] respectively.

Table 2. AKARI IRC flux and color estimates.*

SNR	*N3* (mJy)	*S7* (mJy)	*S11* (mJy)	*L15* (mJy)	*L24* (mJy)	*S11*/*L15*	*L15*/*L24*
0509−67.5	<0.1	<0.2	0.3 ± 0.1	3.9 ± 0.4	20 ± 2	0.08 ± 0.03	0.19 ± 0.03
0519−69.0	<0.6	<1.3	2.5 ± 0.3	33 ± 3	110 ± 11	0.08 ± 0.01	0.30 ± 0.04
N 132 D†	...	...	60 ± 6	980 ± 98	3370 ± 340	0.07 ± 0.01	0.26 ± 0.04
N 49 B	<0.6	<1.6	3.5 ± 0.4	55 ± 5	360 ± 36	0.06 ± 0.01	0.15 ± 0.02
N 49	36 ± 4	280 ± 28	330 ± 33	870 ± 87	1930 ± 193	0.38 ± 0.05	0.45 ± 0.06
SN 1987A	1.5 ± 0.1	4.9 ± 0.5	32 ± 3	43 ± 4	65 ± 7	0.75 ± 0.11	0.66 ± 0.09
N 157 B‡	4.3 ± 0.4	<1.9	39 ± 4	280 ± 28	730 ± 73	0.14 ± 0.02	0.38 ± 0.05
0548−70.4‡	<0.2	<0.6	0.6 ± 0.2	10 ± 1	24 ± 2	0.06 ± 0.02	0.41 ± 0.06

* Fluxes at reference wavelengths of each band are given. The reference wavelengths are 3.2, 7.0, 11.0, 15.0, and 24.0 μm for the *N3*, *S7*, *S11*, *L15*, and *L24*, respectively. *S11* fluxes are from *S11*−*S7* images except N 49 and SN 1987A. Fluxes are not color-corrected. Flux errors are 1σ and limits are 3σ. The last two columns are color ratios of the *S11*/*L15* and *L15*/*L24*.

† N 132 D has not been fully covered in the *S11* band. We derive the *S11* flux by first deriving the ratio of the *S11* to *L15* flux from the shared area and then by multiplying it to the total *L15* flux.

‡ The fluxes of N 157 B and 0548−70.4 are not from the entire SNRs but from the limited areas (figure 3).

figure 5. There is a tight correlation between the two fluxes, as expected, but the *L15*/*L24* flux ratio ranges from 0.15 up to 0.7. The brightest SNRs are N 132 D and N 49. These two SNRs are interacting with their ambient molecular clouds (Banas et al. 1997), and the bright IR emission may be related to the interaction. Type Ia SNRs are the faintest among the identified SNRs with (*L24*, *L15*) = (20, 3.9) to (110, 33) (mJy), while Type II SNRs are located in the upper right part, where (*L24*, *L15*) = (65, 43) to (3370, 980) (mJy).

[4] Preliminary MCELS data are available from the homepage of MCELS, ⟨http://www.ctio.noao.edu/~mcels/⟩.

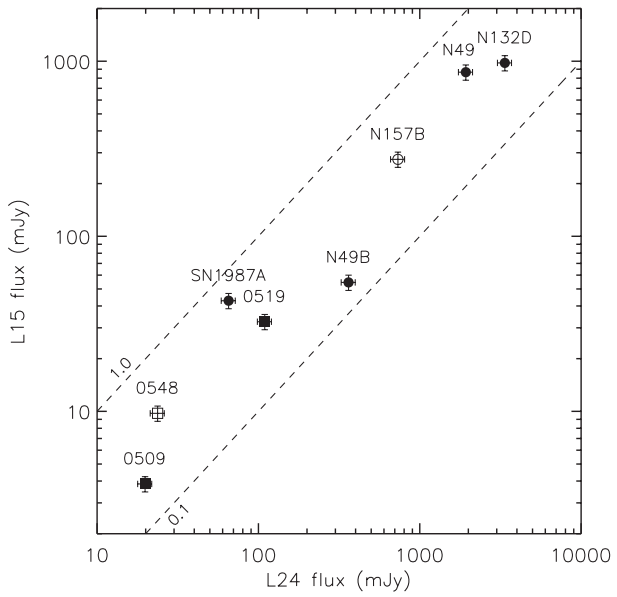

Fig. 5. *L15* flux versus *L24* flux for eight identified SNRs. Square symbols are for Type Ia SNRs and circles for Type II SNRs. Open symbols are for the objects of which fluxes were extracted from limited areas. We use the same symbols hereafter for all plots. Dashed lines show $L15/L24 = 0.1$ and 1.

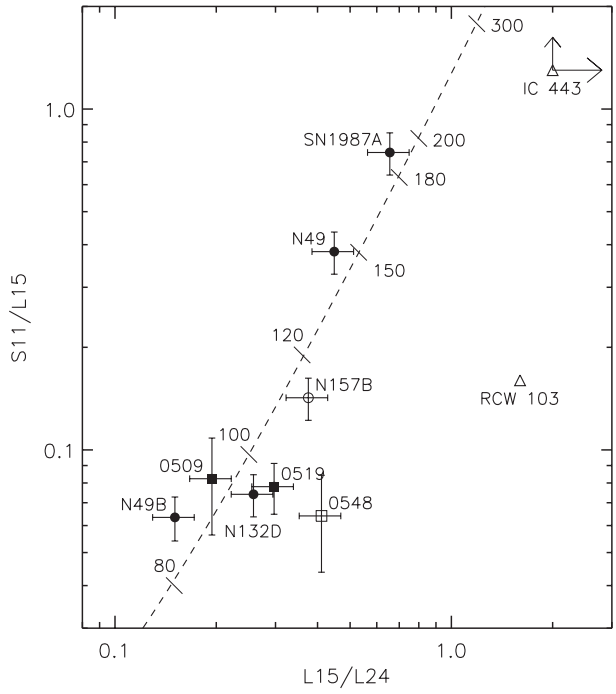

Fig. 6. *S11/L15* flux ratio versus *L15/L24* flux ratio. The dashed line represents the expected ratios from modified blackbody curve of thermal dust emission. Dust temperatures are marked along the line. We also show the synthetic colors of two galactic SNRs, RCW 103 and IC 443 with triangles (see text for an explanation).

3.2. IRC Colors

Figure 6 is a "color–color" diagram comparing the *S11/L15* to *L15/L24* flux ratios. In the figure, the dashed line represents the relation between the flux ratios for thermal dust emission. The dust emission model that we adopt is a single-temperature modified blackbody, where the flux density, F_ν, is given by

$$F_\nu = \frac{\kappa_\nu B_\nu(T_\mathrm{d})}{d^2} M_\mathrm{d}, \quad (1)$$

where T_d is the dust temperature, M_d is the dust mass, κ_ν is the dust mass absorption coefficient, $B_\nu(T_\mathrm{d})$ the Planck function, and d the distance to the LMC, taken to be $d = 51.4$ kpc (Panagia 1999). For the absorption coefficient, we adopt the "average" LMC model of Weingartner and Draine (2001), which consists of mixture of carbonaceous grains and amorphous silicate grains with the maximum carbon abundance being in very small grain population.[5] We also show the synthetic colors of two well-known galactic SNRs, RCW 103 and IC 443, for a comparison. RCW 103 is a young ($\sim 10^3$ yr) SNR with fast ($\gtrsim 300\,\mathrm{km\,s^{-1}}$) shocks interacting with dense CSM/ISM, and its MIR spectrum is dominated by forbidden lines from Ar, Ne, O, and Fe ions (Oliva et al. 1999). On the other hand, IC 443 is a prototype of old SNRs interacting with molecular clouds, and its MIR spectrum is dominated by pure rotational H_2 lines (Neufeld et al. 2007). We synthesized their IRC colors from published spectra to obtain (*L15/L24*, *S11/L15*) = (1.6, 0.16) and (90, 4.3) for RCW 103 and IC 443, respectively.

Figure 6 shows that the MIR flux ratios of the AKARI LMC SNRs are quite different from the two line-dominated galactic SNRs, and are well aligned along the dust-emission line. Note that Type Ia SNRs are located in the lower left part, and SN 1987A has the highest ratios. This good alignment seems to suggest that the MIR emission from these SNRs is, or at least dominated by, thermal dust emission. Indeed, for N 132 D and SN 1987A, the Spitzer spectroscopic observations showed that the contribution from ionic/molecular lines or PAH emission is small in these SNRs (Tappe et al. 2006; Bouchet et al. 2006). Meanwhile, the MIR emission of N 49, which is also lying close to the dust-emission line, has been found to be dominated by ionic lines from shocked gas (R. Williams et al. 2006). However, it is not likely that this mature (~ 6600 yr) remnant would have a sufficiently high dust temperature (~ 150 K) to lie along its position on the dust-emission line. Therefore, although the fact that an SNR is located close to the dust-emission line in figure 6 alone does not assure that its MIR emission is thermal dust continuum emission, the diagram is still helpful to distinguish between line-dominated and dust-dominated SNRs, taking account of their physical contexts. We discuss the origin of the observed MIR emissions in section 5.

4. Comparison with Other Wavebands

4.1. IR vs. X-Rays

Figure 7 compares the AKARI *L24* fluxes (νF_ν) to the X-ray fluxes that are interstellar-absorption corrected X-ray fluxes in the energy range of 0.3 to 2.1 keV. For all MIR detected SNRs, X-ray observations using Chandra are available. To have a homogeneous set of X-ray fluxes for these SNRs, we

[5] Absorption coefficient data files are from the homepage of Bruce T. Draine, available at ⟨http://www.astro.princeton.edu/~draine⟩.

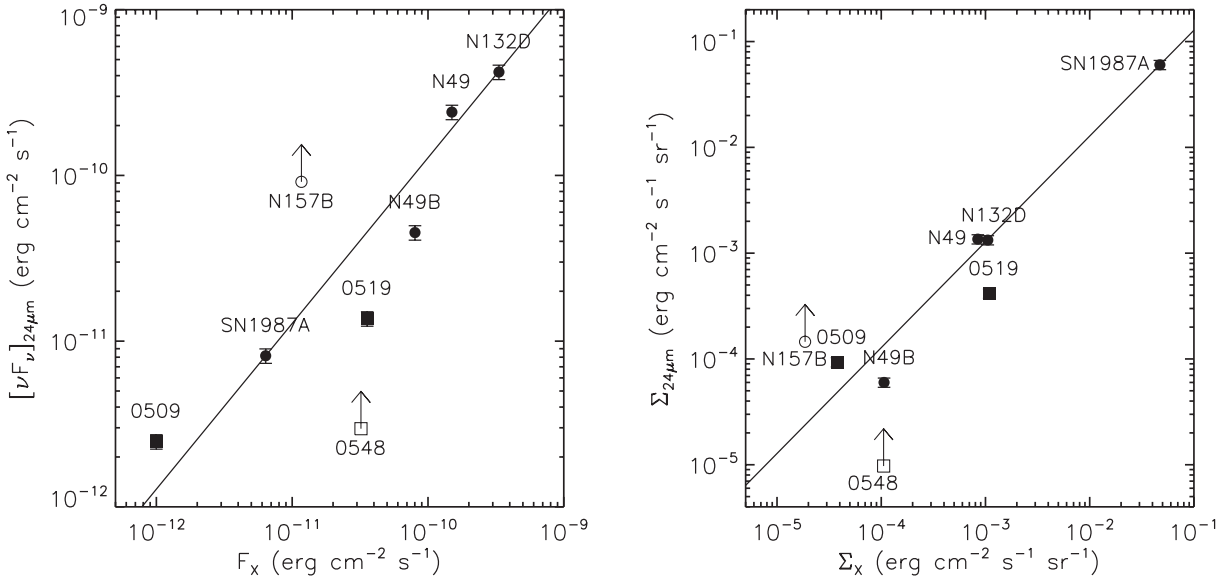

Fig. 7. AKARI 24 μm versus Chandra X-ray (0.3−2.1 keV) fluxes (left) and surface brightness of the SNRs (right). The solid line represents best-fit linear-regression line.

derived the X-ray fluxes of these sources from archival Chandra data. For the intrinsic flux of the source, a correction of the interstellar absorption is required, and the resulting X-ray flux can be sensitive to the assumed hydrogen column density ($N_{\rm H}$). When available, we adopted $N_{\rm H}$ from the literature, and the X-ray flux in the given energy range was estimated by fitting the X-ray spectrum from the archival data. When $N_{\rm H}$ is not readily available from the literature, $N_{\rm H}$ was also derived by fitting the X-ray spectrum. The uncertainty of the intrinsic flux is dominated by the uncertainty in $N_{\rm H}$. We consider our absorption corrected X-ray fluxes will be uncertain by a factor of a few, at most. In the case of SN 1987A, of which the time variation in the X-ray flux is considerably large, we interpolated the latest fluxes from Park et al. (2007) to obtain the X-ray flux corresponding to the AKARI flux. Using the MIR-L and the X-ray data, it was found that there is a good correlation between the two fluxes. Both the *L24* and *L15* fluxes show a good correlation with the X-ray fluxes (correlation coefficient = 0.98 and 0.90, respectively). The relation between the *L24* and X-ray fluxes derived from a linear least-squares fit is

$$[\nu F_\nu]_{24\,\mu{\rm m}} = (1.28 \pm 0.10) \times F_{\rm X}, \quad (2)$$

where $[\nu F_\nu]_{24\mu{\rm m}}$ (erg cm^{-2} s^{-1}) is the flux in the *L24* band and $F_{\rm X}$ (erg cm^{-2} s^{-1}) is the X-ray flux in the 0.3–2.1 keV band. For this and later fits, we did not include N 157 B and 0548−70.4, the fluxes of which were extracted from the limited areas.

The correlation between the two fluxes is expected to some degree, because the IR brightness distributions of the identified SNRs are in general correlated with their X-ray distributions, except for N 157 B. If the MIR emission is dominated by thermal-dust continuum emission, the dust grains emitting the MIR emission are heated by collisions with electrons in the X-ray emitting plasma, so that the two are physically associated, although the flux ratio depends on the plasma temperature, and therefore on the age of the remnant (e.g., Dwek et al. 2008). The correlation in figure 7 (left) is *not* the result of both quantities being proportional to the SNR area. It is shown in figure 7 (right), displaying the surface brightness of the SNRs at 24 μm and X-rays. There is also a good correlation between the surface brightnesses, and the best fit is given as

$$\Sigma_{24\mu{\rm m}} = (1.28 \pm 0.01) \times \Sigma_{\rm X}, \quad (3)$$

where $\Sigma_{24\mu{\rm m}} \equiv [\nu F_\nu]_{24\mu{\rm m}}/\Delta\Omega_{\rm S}$ and $\Sigma_{\rm X} \equiv F_{\rm X}/\Delta\Omega_{\rm S}$, where $\Delta\Omega_{\rm S}$ is the total solid angle of the SNR from table 1. Since the fluxes of N 157 B and 0548−70.4 were derived from limited areas, their surface brightnesses are lower limits. When the MIR emission originates mainly from dust, the dust temperature depends on the density and temperature of electrons. The X-ray flux is proportional to square of the electron density, and at sufficiently high temperature and high densities the dust temperature becomes only dependent on the electron density (Dwek et al. 2008; see subsection 5.1). This suggests that the MIR surface brightness is closely related to the electron density, so that the relationship can lead to the good correlation shown in figure 7.

4.2. *IR vs. Radio*

Figure 8 compares the AKARI *L24* flux (F_ν) to the radio flux at 4.8 GHz. We derived the radio fluxes by using the ATCA 4.8 GHz continuum images of Dickel et al. (2005). We estimated the background intensity using an annulus for most sources. The statistical errors ($1\,\sigma$) of the SNRs are less than 5%. For SN 1987A, due to the time-variability of its radio flux, we applied a flux density gradient (17.5 μJy/day, Manchester et al. 2002) to the observed 4.8 GHz flux (33 mJy in day 5846) in order to obtain the radio flux corresponding to the AKARI flux, i.e., 33 mJy + 17.5 μJy/day × (7190–5846 day) $\simeq$ 56.5 mJy. The scaled flux was used for a further analysis.

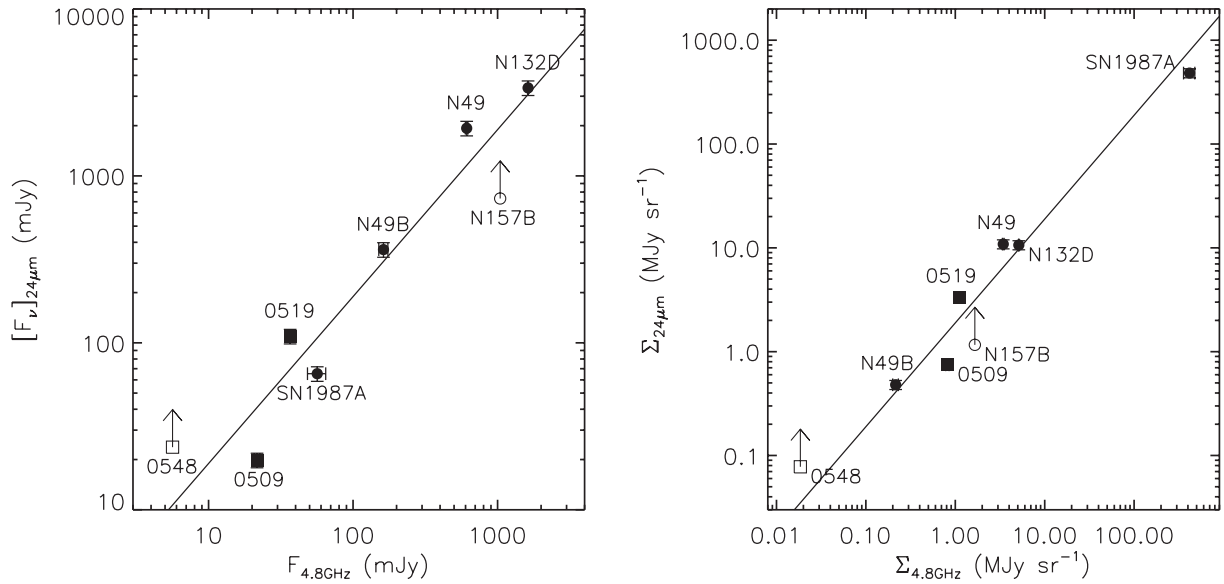

Fig. 8. AKARI 24 μm versus 4.8 GHz radio continuum fluxes (left) and surface brightness (right). The solid line represents best-fit linear regression line.

Figure 8 shows that there is a fairly tight correlation between the two fluxes. The correlation is as good as that between the *L24* and X-ray fluxes (correlation coefficient = 0.98). The relations derived from a least-squares fit are

$$[F_\nu]_{24\mu\mathrm{m}} = (1.89 \pm 0.09) \times F_{4.8\,\mathrm{GHz}} \quad (4)$$

and

$$\Sigma_{24\mu\mathrm{m}} = (1.89 \pm 0.09) \times \Sigma_{4.8\,\mathrm{GHz}}, \quad (5)$$

where $F_{4.8\,\mathrm{GHz}}$ (erg cm^{-2} s^{-1} Hz^{-1}) is the radio flux at 4.8 GHz and $\Sigma_{4.8\,\mathrm{GHz}} \equiv F_{4.8\,\mathrm{GHz}}/\Delta\Omega_\mathrm{S}$ is the radio surface brightness at 4.8 GHz.

The correlation between the *L24* and radio fluxes in figure 8 is remarkable, considering that there is no direct physical connection between the IR and the radio synchrotron emission. The synchrotron emission is due to the compression of electrons and magnetic fields in the ISM, except for the pulsar wind nebula N 157 B. The contribution of synchrotron emission to the observed 24 μm emission should be negligible. Thus, the apparent correlation between the two fluxes in figure 8 could be due to their common dependence on the physical parameters of SNRs, such as the shock velocity and the ambient density. We note that Type Ia SNRs are faint in both IR and radio (and X-rays too), while the SNRs probably interacting with nearby molecular clouds are bright in both bands. Since Type Ia SNRs are expected to be in a lower-density environment, this trend indicates that one of the most important factors for detection in IR is likely to be the density of the ambient medium.

The correlation in figure 8 would be compared to that among galaxies. It has been known for over three decades that there is a tight correlation between the far-infared and radio emissions from galaxies, and recent Spitzer studies have showed that even MIR and radio have a fairly good correlation ($F_{24\mu\mathrm{m}}/F_{1.4\,\mathrm{GHz}} \sim$ 7–25: Appleton et al. 2004; Boyle et al. 2007). For a comparison, the correlation in figure 8 implies 24 μm to 1.4 GHz flux ratios of 1.0 using a spectral index of -0.5 for radio synchrotron emission. Therefore, if the 1.4 GHz radio emission from galaxies is mainly from SNRs, the contribution of SNRs to the 24 μm fluxes from galaxies would be 4–14%, the rest of which might be contributed from star-formation activity.

5. Discussion

5.1. *Origin of Infrared Emission*

There are generally four sources of the MIR (10–30 μm) emission in SNRs: ionic and/or molecular lines, thermal dust continuum emission, PAH bands, and non-thermal synchrotron emission (Koo et al. 2007 and references therein). Synchrotron emission is usually negligible, except for young PWN, such as Crab Nebula. PAH emission has not been detected towards SNRs, except for N 132 D where it appears as a 15–20 μm emission hump superposed on a strong dust continuum (Tappe et al. 2006). It is usually either the thermal emission from collisionally-heated dust grains in hot plasma or forbidden lines from such elements as Ne, O, Fe ions and pure rotational H_2 lines that dominate the emission in this wave band. In order to distinguish between line- and dust-dominated SNRs, we can compare an IR color of a SNR to a theoretical prediction from the main emission mechanisms in a color–color diagram. Besides this, a comparison of the IR morphology to X-ray and optical can be another useful means. When the IR morphology is very similar to that of X-rays, but optical, this might indicate that thermal dust emission is dominant in a SNR because, if the line radiation from a radiative shock is dominant, the IR morphology would be similar to the optical. However, in the case of a Balmer-dominated SNR, the resemblance between IR and optical often appears to be as good as that between IR and X-rays, so that other physical conditions such as age, should also be considered.

For three Type II SNRs, N 132 D, SN 1987A, and N 49, spectroscopic observations have been made using Spitzer. It is shown that the MIR spectra (10–30 μm) of the former two SNRs are dominated by the thermal dust continuum with a small contribution from several ionic lines and PAH emission (Tappe et al. 2006; Bouchet et al. 2006; Dwek et al. 2008). Their AKARI MIR colors are consistent with these spectroscopic results (see next). On the other hand, the MIR spectrum of N 49 is found to be dominated by ionic lines from shocked gas without any substantial dust continuum emission (R. Williams et al. 2006). (There are some pure rotational H_2 lines too, but their contribution is relatively small.) This is interesting because the AKARI MIR colors of N 49 are aligned close to those of thermal dust emission (figure 6). We checked the possibility that the MIR spectra of the positions where the spectroscopic observations were performed do not represent the spectrum of the entire SNR in N 49. The spectroscopic observations were performed toward two positions, and their synthetic IRC colors are (*L15*/*L24*, *S11*/*L15*) = (0.41, 0.26) and (0.23, 0.28), respectively. For a comparison, the observed IRC color of the entire SNR N 49 is $\sim$(0.45, 0.38), which is not significantly different from the synthetic ratio.[6] The somewhat higher *S11*/*L15* ratio could be either due to variations of the line intensities over the remnant, or possibly due to dust emission. The important point is that the SNRs dominated by ionic line emission can have colors similar to modified blackbodies in the (*L15*/*L24*, *S11*/*L15*) diagram. Important lines in these bands are [Ne II] 12.81 μm (*S11*), [Ne III] 15.56 μm (*L15*), [O IV] 25.90 μm, and [Fe II] 26.00 μm (*L24*) lines. RCW 103 is far off from the modified blackbody line, apparently because its Ne lines are much stronger than O or Fe lines, in contrast to N 49.

For the other five SNRs, no MIR spectroscopic data are available at the moment. For 0509−67.5 and 0519−69.0, Spitzer recently obtained their spectra, which have not been released yet, and an IRS observation of N 157 B is also planned; 0509−67.5 and 0519−69.0 are young, Balmer-dominated Type Ia SNRs. Their shock is very fast ($\gtrsim$3000 km s^{-1}) and non-radiative (Ghavamian et al. 2007), so that we do not expect strong IR ionic or molecular line emission. Their MIR emission might be from shock-heated dust grains. The other Type Ia SNR, 0548−70.4, is also Balmer-dominated, but significantly older ($\sim 7 \times 10^3$ yr) (Hendrick et al. 2003). An interesting feature of this remnant is the X-ray emitting gas in the central region, where the bright MIR emission is detected by AKARI (figure 3). It shows enhanced metal abundance, and could be SN ejecta swept-up by reverse shock (Hendrick et al. 2003). On the other hand, there are bright Hα/[O III]-emitting clumps mixed with X-ray emitting gas, and they could be either dense ejecta or interstellar clumps swept up by slow, radiative shocks (cf. Ghavamian et al. 2007). The brightness distribution of the MIR emission is considerably different from the X-rays. There are several bright clumps seen in the X-rays, and some of them are extended towards the south, where there is no distinct MIR emission. Instead, the optical knots in the Hα images are mainly distributed inside of the central MIR emitting region. This remnant is also considerably off from the thermal dust-emission line in figure 6. This suggests that the MIR emission in the central area is likely to be dominated by ionic lines from radiative shocks, rather than by continuum emission from hot dust.

[6] The referee pointed out that, according to her/his recent spectral mapping of N 49, there are faint signs of continuum emission in some remnant regions, but line emission is a strong contributor in all IR-bright areas of this SNR. This supports our argument.

Table 3. Dust properties of five SNRs.*

SNR	T(dust) (K)	$L_{\rm IR}$ (erg s^{-1})	Dust mass ($M_\odot$)
0509−67.5	94 ± 3	8.1×10^{35}	$8.7 \pm 2.5 \times 10^{-5}$
0519−69.0	99 ± 4	4.5×10^{36}	$3.6 \pm 1.0 \times 10^{-4}$
N 132 D	96 ± 4	1.4×10^{38}	$1.3 \pm 0.3 \times 10^{-2}$
N 49 B	86 ± 3	1.6×10^{37}	$2.8 \pm 0.7 \times 10^{-3}$
SN 1987A	185 ± 15	3.6×10^{36}	$1.0 \pm 0.2 \times 10^{-5}$

* Probably dominated by thermal dust emission.

Two remaining SNRs are N 49 B and N 157 B, both of which are Type IIs. N 49 B is a middle-aged shell-type SNR, and its MIR morphology is very similar to the X-rays whereas the Hα image hardly shows any shell structure (R. Williams et al. 1999). This suggests that the MIR emission is likely dominated by thermal dust emission. But the bright portion of the southern shell and also the clump in the eastern part appear to be bright in Hα/[O III] emission (Mathewson et al. 1983), so that there could be some contribution from ionic line emission. N 157 B is a Crab-like SNR. As we described in subsection 3.1, we have not detected any appreciable IR emission corresponding to the PWN, but detected IR emission corresponding to the Hα-emitting nebula in the east of the PWN, both in MIR and NIR bands (figures 3–4; cf. R. Williams et al. 2006). The MIR emission is probably dominated by ionic lines. In summary, among 5 SNRs, the MIR emissions of 0509−67.5, 0519−69.0, and N 49 B are thought to be dominated by thermal dust continuum, while 0548−70.4 and N 157 B are by ionic lines.

For SNRs that are considered to be dominated by thermal dust emission, we fit their AKARI *S11*, *L15*, and *L24* fluxes by a single-temperature dust emission; the results are summarized in table 3. For this calculation, we first color-corrected the measured fluxes by assuming a modified blackbody curve [equation (1)]. The correction factors ranged over 0.8–1.1, 1.3–2.3, and 0.9–1.1 for the *S11*, *L15*, and *L24*, respectively. Note that the correction factors of the *L15* band are large because the dust mass absorption coefficient, κ_ν, in the assumed model has a dip near 15 μm, owing to the characteristics of the silicate. The derived temperatures vary from 86 to 185 K, which corresponds to luminosity and mass ranges of 0.8–140 $\times 10^{36}$ erg s^{-1} and 0.1–130 $\times 10^{-4}$ $M_\odot$. The derived temperatures agree with the results derived from the Spitzer spectroscopy on the N 132 D and SN 1987A. For N 132 D, Tappe, Rho, and Reach (2006) applied a two-component fit to its Spitzer IRS spectrum of the southeastern rim to derive temperatures of 58 K and 110 K. The higher temperature component contributes most of the emission at $\lesssim$30 μm. Our temperature (96 K) is somewhat lower than their 110 K, but this could be due to the lower-temperature component. For SN 1987A, Bouchet et al. (2006) and Dwek et al.

(2008) showed that its Spitzer IRS spectrum is well described by a single-temperature thermal dust emission at ~ 180 K.

Dust grains in hot plasma are mainly heated by collisions with electrons. The dust temperature depends on the electron temperature and the density. When the plasma temperature is sufficiently high, most electrons go through dust grains, and the dust temperature becomes dependent only on the electron density (Dwek et al. 2008). Dwek et al. (2008) showed that 0.023–0.22 μm-sized dust grains in the hot plasma at 3.5×10^6 K with a density of (0.3–1) $\times 10^4$ cm^{-3} can reach 180 K, the temperature observed in SN 1987A. The dust temperatures of the other four SNRs are 86–99 K. Such temperatures can be achieved for 0.01–0.1 μm-sized dust grains in a hot plasma at $\sim 10^7$ K when the electron density is higher than 10–20 cm^{-3}. We note that for Type II SNRs (N 132 D and N 49), X-ray observations indicated such high densities (R. Williams et al. 2006; Park et al. 2003). For two Type Ia SNRs (0509−67.5 and 0519−69.0), an analysis of Hα lines yielded lower limits on the electron densities, 1.6 cm^{-3} and 7.7 cm^{-3} (Borkowski et al. 2006). The MIR emissions in these remnants are mostly from confined regions, and it is possible that these regions are where the blast wave is propagating into dense interstellar material of higher electron density.

5.2. *Dust Destruction by SNR Shocks*

SNR shocks are the main source of dust destruction. Dust grains are destroyed by sputtering and grain–grain collisions behind the shock (Jones 2004). Recently, Borkowski et al. (2006) and B. Williams et al. (2006) observed Type Ia and core-collapse SNRs using Spitzer, respectively. They found that dust destruction by sputtering is necessary to reproduce the observed 70/24 μm ratios according to their shock model calculation. They concluded that about 40% of the mass in dust grains has been destroyed, and smaller grains (≤ 0.04 μm) have been shattered up to 90% in both types of SNRs.

We note that the dust temperatures derived from the AKARI *S11*, *L15*, and *L24* fluxes are considerably higher than those of Borkowski et al. (2006) and B. Williams et al. (2006). If we calculate the 70/24 μm flux ratios using our dust temperature, the ratios are significantly smaller than the Spitzer results. This is shown in figure 9, which is a color–color diagram of AKARI *L15*/*L24* versus Spitzer 24/70 μm. Spitzer 24/70 μm ratios are adopted from the literature (Borkowski et al. 2006; B. Williams et al. 2006; R. Williams et al. 2006). It is clear that a single temperature cannot describe the full spectral energy distribution (SED) of these SNRs, including those probably dominated by thermal dust emission. It is interesting that N 49 and 0548−70.4, two SNRs thought to be line-dominated, deviate more from the dust-continuum curve. From previous studies, it is known that the SED of SNRs usually requires two components, cold and warm dust. We can also explain the color of SNRs in figure 9 with an extra cold component at 20–40 K and with the mass ratio to the warm component of 50–1000. The lines in figure 9 show the cases when the temperature of the cold component is 30 K and 40 K and the mass ratio is 500. The colors of the line-dominated SNRs, however, cannot be easily described by an extra cold component. We can fit their colors using a cold component (30–40 K) plus a warm component (100–150 K) with a mass ratio of ~ 10000. But,

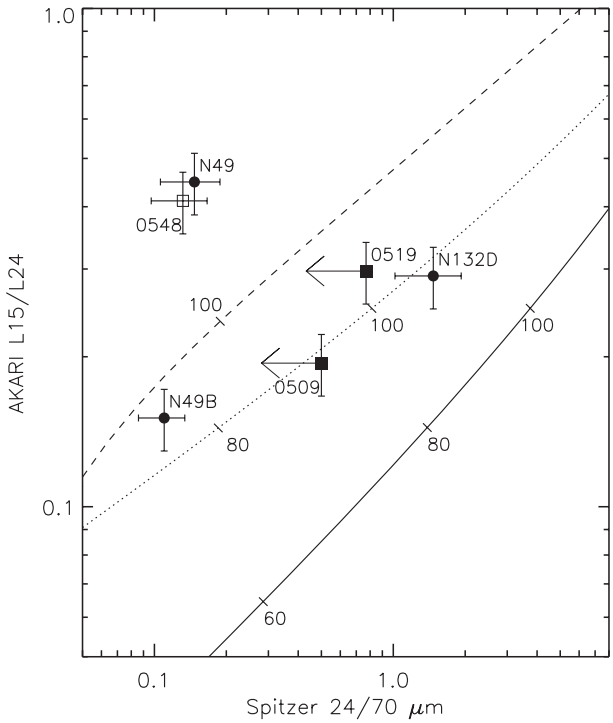

Fig. 9. AKARI *L15*/*L24* flux ratio versus Spitzer 24/70 μm flux ratio. The solid line represents the expected ratios from a modified blackbody curve of thermal dust emission with a single component. The dotted and dashed lines show the ratios of two-component dust emission with $T_{\rm cold} = 30$ K and 40 K, respectively when $M_{\rm cold}/M_{\rm warm} = 500$ (see text for detail).

since both SNRs are middle-aged, the temperature of the warm component appears to be too high for them. This supports our conclusion that these SNRs are line-dominated. The strong ionic lines around 70 μm are [O I] 63 μm and [O III] 88 μm, which might have caused the 24/70 μm ratio to decrease. This might indicate that the discrepancy is to some extent due to the line emission.

Multiple dust temperatures could happen if the ambient ISM is clumpy, so that the shock velocities and therefore the dust temperatures, differ for the clump and interclump medium, as suggested by Tappe, Rho, and Reach (2006) in N 132 D. It can also happen if the grains size distribution does not follow a simple power law. In this regard, it is worth noting that previous IRAS studies showed that the IR emission from SNRs usually require two components: a cold component dominating $\gtrsim 70$ μm and a warm component dominating $\lesssim 25$ μm (Arendt 1989; Saken et al. 1992). Figure 9 is consistent with previous IRAS results, and suggests that the 70 μm fluxes in these SNRs might be dominated by the cold dust component. This result implies that the destruction rate of grains in these SNRs may not be as high as previously estimated from the 24/70 μm flux ratios.

6. Summary

We performed an IR study of 21 LMC SNRs listed in table 1 using the AKARI IRC survey data. We systematically

examined the AKARI images in the 3 μm (*N3*), 7 μm (*S7*), 11 μm (*S11*), 15 μm (*L15*), and 24 μm (*L24*) bands, and detected eight SNRs with associated IR emission (table 2). In the *S11* band, we could reveal the SNR features much more clearly by subtracting the background emission using the *S7* band image. We summarize our main results below:

1. In all eight sources, we can see distinct MIR emission features at the position of SNRs in the *S11*, *L15*, and *L24* bands. Our *L24* images are consistent with their Spitzer 24 μm images. The *S11* and *L15* images are new in these wavebands, and show that individual SNRs have compatible morphologies in three bands. This suggests that the MIR emissions in these three bands are of the same origin. In shorter wavebands, three SNRs are clearly visible: N 49, SN 1987A, and N 157 B.

2. In the *S11*/*L15* flux ratio versus the *L15*/*L24* flux ratio diagram, the SNRs are well-aligned along a track of thermal dust emission. Type Ia SNRs are located in the lower left with low ratios, while Type II SNRs are spread from low to high ratios. SN 1987A has the highest ratios. The alignment along the dust emission line does not necessarily imply that the origin of the MIR emission is thermal dust continuum, because the SNRs dominated by ionic lines can have colors similar to modified blackbodies in this diagram. But the diagram is still helpful to distinguish between line-dominated and dust-dominated SNRs, while taking account of their physical contexts.

3. The flux in the *L24* band has a good correlation with both the soft X-ray and radio fluxes. There is also a good correlation between the corresponding surface brightnesses. The correlation between the MIR and radio is remarkable, considering that there is no direct physical connection between the two. The correlations might be due to their common dependence on the physical parameters of SNRs, particularly the density of the ambient medium. The correlation yields $\sim$1.0 for the ratio of 24 μm to 20 cm radio fluxes of SNRs, and it implies that the contribution of SNRs to the 24 μm fluxes from galaxies would be 4%–14% at most.

4. We consider that the MIR emission from the five SNRs is dominated by thermal dust emission: two Type Ia SNRs (0509−67.5 and 0519−69.0) and three Type II SNRs (N 132 D, N 49 B, and SN 1987A). We derived dust temperatures of $\sim$90–190 K from their 10–25 μm fluxes. Their *L15*/*L24* color temperatures are generally higher than the Spitzer 24/70 μm color temperatures, which suggests that the dust emission model at single equilibrium temperature cannot describe the full SED of these SNRs. This also implies that understanding the full SED is essential for estimating the dust destruction rate of grains by SNR shocks.

This work is based on observations with AKARI, a JAXA project with the participation of ESA. We wish to thank all the members of the AKARI project. We thank an anonymous referee for helpful comments, which have considerably improved the paper. We also would like to thank Snezana Stanimirovič for useful comments on the IR/radio correlation of galaxies. This work was supported by the Korea Science and Engineering Foundation (R01-2007-000-20336-0) and the Korea Research Foundation (R14-2002-058-01003-0).

Appendix. Brief Description on Individual SNRs

0509−67.5 — This Balmer-dominated remnant is one of the youngest SNRs in the LMC, and its X-ray spectra indicate that it originated from a Type Ia SN explosion (Hughes et al. 1995). There is a bright, elongated feature southwest of the SNR in the MIR-L bands, which coincides with the brightest portion of the shell structure seen in both the X-ray and optical images (Borkowski et al. 2006). *S11* and *S11*−*S7* images also show emission at the same position. Because it is faint, the morphologies in the *S11* and *S11*−*S7* are not clear. In addition to the bright southwestern limb, in the *L24*, the faint emission from the rest of the SNR is visible, as seen in X-rays and optical. The bright point-like source just outside the southwestern boundary of the contour in the *S11* is a background source (2MASS J05092882−6731307).

0519−69.0 — This is another young Balmer-dominated SNR, which probably originated from a Type Ia SN explosion (Hughes et al. 1995; Ghavamian et al. 2007). The shell structure, well-defined in Hα and X-rays, is clearly seen in the MIR-L bands. Also, it shows three bright knots in the north (N), east (E), and southwest (SW) along the limb. While only the N and the E knots are visible in the *S11* image, all three knots are clearly visible in the *S11*−*S7* image with the morphology nearly identical to those of the MIR-L. The N and the E knots spatially correspond to the relatively bright region in X-rays and Hα, whereas the SW knot does not have specific counterpart in those bands. This discrepancy of the knots indicates the different characteristics among them.

N 132 D — This SNR belongs to young oxygen-rich SNRs that are the product of the core-collapse SNe (Morse et al. 1995). The remnant is one of the brightest LMC SNRs, and shows a well-defined shell structure in the MIR bands as in the X-rays. The southeastern (SE) rim contains enhanced IR emission which might be caused by the interaction with a molecular cloud in this area (Banas et al. 1997; Tappe et al. 2006). Only the bright SE shell is visible in the *S11* band together with the northwestern knot named "West Complex" by the previous optical observation (Tappe et al. 2006). However, the *S11*−*S7* image shows the morphology just same as that of the MIR-L bands. The central bright emission in the *S11* band, showing weak correlation with X-rays, might be mainly attributed to background emission. The IR morphology is somewhat different from that of the optical, which shows a relatively fainter shell compared to the bright ejecta region at the center (Borkowski et al. 2007). Using the Spitzer IRS observations, Tappe, Rho, and Reach (2006) revealed the dominant dust continuum with the first detected PAH emission.

N 49 B — This is a middle-aged SNR of core-collapse SN origin (Hughes et al. 1998; Park et al. 2003). The SNR shell is clearly seen in the MIR-L bands, and its morphology is similar to that in X-rays. The SNR has several patchy emission along the limb including the particularly bright southern rim in the MIR-L bands. There is some diffuse IR emission in the inner region with a belt-like feature crossing the shell. Even though the *S11* image does not show prominent emission related to the SNR, the *S11*−*S7* image reveals some emission, such as the southern rim, a belt-like feature, and a northwest shell similar to the features in the MIR-L bands.

N 49 — This Type II SNR is unique in showing very strong emission in all IRC bands. Previous X-ray and radio observations show fairly clear emission over the entire shell of the SNR with the peak in the east (R. Williams et al. 2006). While the IRC images also show the similar morphology, the IR peak has a different position from the X-rays/radio. Besides, the SNR has a lack of IR emission in the northwest, unlike the X-rays/radio, although the complete shell of the X-rays/radio is marginally detected in the MIR-L bands. A bright wedge-shaped feature in the east is clearly visible in all IRC bands, which is quite similar to that seen in the HST observations (Bilikova et al. 2007). Also, the overall IR morphology has good correspondence to that of optical. In the *S7* band, there appears a protrusion that extends to the east from the wedge-shaped filament. Since the structure extends beyond the SNR boundary, it is not likely to be physically associated with the SNR. But it is worth to note that it is spatially coincident with the ambient molecular cloud possibly interacting with the SNR (Banas et al. 1997).

SN 1987A — This newly formed SNR has just started its interaction with dense circumstellar material around the inner ring (e.g., Park et al. 2005). The effect of this encounter has been detected as a rapid brightness change at various wavelengths including IR (Bouchet et al. 2006). AKARI observed this SNR at 2006 October 31–November 4 (days 7190–7194) and the estimated flux agrees with the IR flux variation found by the recent Spitzer study (Dwek et al. 2008). The remnant appears to be point-like in all IRC bands, but the previous observation with higher resolution shows a resemblance with X-rays, rather than optical in terms of the brightness distribution (e.g., see figures 3 and 16 in Bouchet et al. 2006). The ring-like feature around the SNR in the MIR-L bands is the shape of point-spread-function (PSF) of the IRC.

N 157 B — This remnant is one of the two known Crab-like SNRs in the LMC. No appreciable IR emission related to the pulsar or PWN has been detected. The bright emission is mostly originated not from the SNR, but from nearby sources, including a small molecular cloud in the south (Johansson et al. 1998), possibly undergoing star-forming activities in progress. However, it is found that there are some features, such as the horseshoe-shaped one and arm-like emission, towards the northeast in all IRC bands, except for *S7*. These features correspond well to the Hα emission of the SNR observed by Chu et al. (1992). This indicates they are associated with N 157 B.

0548−70.4 — This middle-aged ($\sim$ 7000 yr), Balmer-dominated SNR has been categorized into a Type Ia remnant because its observed ratio of oxygen to iron is much lower than that from typical core-collapse SNe (Hendrick et al. 2003). The shell structure detected in Hα and X-rays is not clearly seen in the IRC images, while the Spitzer image shows an outer shell similar to the Hα/X-rays, owing to its higher resolution (Borkowski et al. 2006). Nevertheless, there is a distinct emission in MIR bands that has a spatial correspondence to the central region with X-ray emission. While the overall shape of the IR emission is similar to that of the X-rays, its brightness distribution is quite different from the X-rays. Instead, the brightness distribution of MIR emission seems to be closer to the Hα including the bright knot at the center.

References

Appleton, P. N., et al. 2004, ApJS, 154, 147
Arendt, R. G. 1989, ApJS, 70, 181
Banas, K. R., Hughes, J. P., Bronfman, L., & Nyman, L.-A. 1997, ApJ, 480, 607
Bilikova, J., Williams, R. N. M., Chu, Y.-H., Gruendl, R. A., & Lundgren, B. F. 2007, AJ, 134, 2308
Blair, W. P., Ghavamian, P., Long, K. S., Williams, B. J., Borkowski, K. J., Reynolds, S. P., & Sankrit, R. 2007, ApJ, 662, 998
Borkowski, K. J., et al. 2006, ApJ, 642, L141
Borkowski, K. J., Hendrick, S. P., & Reynolds, S. P. 2007, ApJ, 671, L45
Bouchet, P., et al. 2006, ApJ, 650, 212
Boyle, B. J., Cornwell, T. J., Middelberg, E., Norris, R. P., Appleton, P. N., & Smail, I. 2007, MNRAS, 376, 1182
Chu, Y.-H., Kennicutt, R. C., Jr., Schommer, R. A., & Laff, J. 1992, AJ, 103, 1545
Dickel, J. R., McIntyre, V. J., Gruendl, R. A., & Milne, D. K. 2005, AJ, 129, 790
Dwek, E., et al. 2008, ApJ, 676, 1029
Ghavamian, P., Blair, W. P., Sankrit, R., Raymond, J. C., & Hughes, J. P. 2007, ApJ, 664, 304
Graham, J. R., Evans, A., Albinson, J. S., Bode, M. F., & Meikle, W. P. S. 1987, ApJ, 319, 126
Hendrick, S. P., Borkowski, K. J., & Reynolds, S. P. 2003, ApJ, 594, 370
Hughes, J. P., et al. 1995, ApJ, 444, L81
Hughes, J. P., Hayashi, I., & Koyama, K. 1998, ApJ, 505, 732
Ita, Y., et al. 2008, PASJ, 60, 435
Johansson, L. E. B., et al. A&A, 331, 857
Jones, A. P. 2004, in ASP Conf. Ser., 309, Astrophysics of Dust, ed. A. N. Witt, G. C. Clayton, & B. T. Draine (San Fransisco: ASP), 347
Kim, S. 1998, PhD Thesis, Australian National University
Koo, B.-C., et al. 2007, PASJ, 59, S455
Lazendic, J. S., Dickel, J. R., Haynes, R. F., Jones, P. A., & White, G. L. 2000, ApJ, 540, 808
Manchester, R. N., Gaensler, B. M., Wheaton, V. C., Staveley-Smith, L., Tzioumis, A. K., Bizunok, N. S., Kesteven, M. J., & Reynolds, J. E. 2002, PASA, 19, 207
Mathewson, D. S., Ford, V. L., Dopita, M. A., Tuohy, I. R., Long, K. S., & Helfand, D. J. 1983, ApJS, 51, 345
Meixner, M., et al. 2006, AJ,132, 2268
Morse, J. A., Winkler, P. F., & Kirshner, R. P. 1995, AJ, 109, 2104
Neufeld, D. A., Hollenbach, D. J., Kaufman, M. J., Snell, R. L., Melnick, G. J., Bergin, E. A., & Sonnentrucker, P. 2007, ApJ, 664, 890
Oliva, E., Moorwood, A. F. M., Drapatz, S., Lutz, D., & Sturm, E. 1999, A&A, 343, 943
Onaka, T., et al. 2007, PASJ, 59, S401
Panagia, N. 1999, in IAU Symp., 190, New Views of the Magellanic Clouds, ed. Y.-H. Chu, N. Suntzeff, J. Hesser, & D. Bohlender (San Francisco: ASP), 549
Park, S., Burrows, D. N., Garmire, G. P., McCray, R., Racusin, J. L., & Zhekov, S. A. 2007, AIP Conf. Proc., 937, 43

Park, S., Hughes, J. P., Slane, P. O., Burrows, D. N., Warren, J. S., Garmire, G. P., & Nousek, J. A. 2003, ApJ, 592, L41
Park, S., Zhekov, S. A., Burrows, D. N., & McCray, R. 2005, ApJ, 634, L73
Saken, J. M., Fesen, R. A., & Shull, J. M. 1992, ApJS, 81, 715
Smith, C., Leiton, R., & Pizarro, S. 2000, ASP Conf. Proc., 221, 83
Tappe, A., Rho, J., & Reach, W. T. 2006, ApJ, 653, 267
Weingartner, J. C., & Draine, B. T. 2001, ApJ, 548, 296
Williams, B. J., et al. 2006, ApJ, 652, L33
Williams, R. M., Chu, Y.-H., Dickel, J. R., Petre, R., Smith, R. C., & Tavarez, M. 1999, ApJS, 123, 467
Williams, R. M., Chu, Y.-H., & Gruendl, R. 2006, AJ, 132, 1877